Particle impaction on a cylinder in a crossflow as function of Stokes and Reynolds numbers

NILS ERLAND L. HAUGEN AND STEINAR KRAGSET†

SINTEF Energy Research, N-7465 Trondheim, Norway

A high-order direct numerical simulation code (THE PENCIL CODE) has been used together with the immersed boundary method on a Cartesian grid to simulate particle impaction on a cylinder in a crossflow. The direct numerical scheme concerns only the fluid flow, into which the particles are subsequently coupled through a one-way drag-coefficient law. The immersed boundary method is extended to work with high-order discretization, and the particle impaction efficiency has been measured for Stokes numbers ranging from 0.001 to 40 for a range of different Reynolds numbers. Three modes of impaction on the front side of the cylinder are identified, where, for the large-Stokes-number mode ($St > 0.3$), an alternative to the traditional Stokes number is presented that provides better scaling. The intermediate impaction mode has a very steep decrease in impaction efficiency as the Stokes number is decreased, and this is identified as the range of Stokes numbers where the viscous boundary layer starts to take effect. The third mode of front-side impaction is for the very small particles with $St < 0.1$ exactly following the flow but impacting on the cylinder due to their finite radii. There will not be any capture on the front side of the cylinder for impact angles larger than $\sim 56°$ for this mode. Finally, it is found that the particle impaction on the back side of the cylinder is strongly dependent on the flow Reynolds number, where large Reynolds numbers lead to larger impaction efficiencies. The upper limiting Stokes number of back-side impaction is around 0.13, apparently irrespective of the Reynolds number.

Key words: complex fluids, computational methods, particle/fluid flows

---

1. Introduction

The motivation for the first studies of inertial impaction of particles onto some solid object was an acute shortage of materials for air filters in Germany during World War I. Since then much effort has been put into this study worldwide due to its importance in a large variety of different applications such as filters, furnaces, industrial boilers and icing on aerofoils. In the first of these applications, developers are interested in maximizing the total particle deposition, while in all of the other applications mentioned above, the aim is always to minimize the deposition.

There are two requirements for a particle to deposit on a surface; firstly, the particle must get in physical contact with the surface, and secondly, it must stick to the surface. The first requirement is measured by the particle impaction efficiency, which determines the fraction of the particles initially moving in the direction of the

† Email address for correspondence: steinar.kragset@sintef.no

solid obstacle that really collide with the object. The second requirement is determined by the particle adsorption or sticking coefficient, which again is a variable of several different conditions such as the melt fraction of the particle, any electric force or different kinds of contact forces such as van der Waals forces.

This study focuses on inertial impaction. Other particle impaction mechanisms, such as Brownian motion, thermophoresis, turbulent eddy diffusion and electrophoresis, are not considered here. The reason for omitting these mechanisms is that they are all less general than inertial impaction in that they all depend on variables such as temperature, turbulence or any sort of electric field. For the same reason, particle concentration is not an issue here, and this study focuses on the single-particle behaviour rather than including particle–particle or particle–fluid interactions. Besides, in typical industrial boilers, relatively low particle concentrations are found in the flue gases, making the single-particle behaviour relevant.

Following the laws of Newton, a particle will move in a straight line unless acted upon by a force. This is due to the particle inertia. The larger the inertia, the larger the force required to deflect the particle by a certain amount from its original path. Consequently, if there are no forces acting on the particle, a particle initially moving in the direction of the obstacle will also reach the obstacle, leading to a particle impaction efficiency of

$$\eta_{no\ force} \equiv 1 + R_i. \tag{1.1}$$

The particle efficiency is normalized to unity when counting all particles whose centres of mass are initially moving in the direction of the solid object of size D. Since additional particles will be intercepted due to their finite size d_p, the interception parameter $R_i = d_p/D$ is added to yield a maximum particle impaction efficiency that exceeds unity (Kasper *et al.* 2009).

If the particles are immersed in a fluid flow, the flow will be deflected by the obstacle, and the particles will experience a drag force. This force will always try to accelerate the particles into the same velocity as the fluid flow, and therefore lead to an impaction efficiency smaller than $\eta_{no\ force}$. In most theoretical approaches to this subject, the fluid flow is calculated on the basis of potential-flow theory. This approach is extremely attractive in that there exists an analytical description for the fluid velocities at every point in the domain. By utilizing this approach, Israel & Rosner (1983) present a curve fit for the impaction efficiency as a function of the Stokes number (the Stokes number is defined in (3.5) and relate the time scale associated with the particle motion to the time scale of the fluid flow). Later, Baxter (1990) published a similar fit with modified fitting coefficients. By using the full nonlinearized equations, Ingham, Hildyard & Heggs (1990) found the limiting Stokes number, below which there will not be any capture, to be 1/12 with the potential-flow approach. Furthermore, they found that when allowing for viscid flows there is no limiting Stokes number.

The two most cited communities within the field of particle deposition on single cylinders are the filter community (Suneja & Lee 1974; Muhr 1976; Schweers, Umhauer & Löffler 1994; Kasper *et al.* 2009), and the industrial boiler community (Loehden *et al.* 1989; Huang *et al.* 1996; Yilmaz & Cliffe 2000; Li, Zhou & Cen 2008). But in none of these studies have we been able to find any reference to very small-Stokes-number deposition. For this reason, we will focus a relatively large part of this study on the small-Stokes-number deposition.

Since the boundary layer is very important for the deposition of particles with small Stokes numbers, it is necessary to use direct numerical simulations (DNS) to

resolve the full boundary layer. Here, DNS is understood as simulations where the Navier–Stokes equations have been solved without the use of any kind of modelling such as turbulence models or wall models. In our DNS code, we do not use any artificial filtering, and since we use a high-order discretization scheme, the numerical diffusion is negligible such that the only sink of small-scale structures is the kinematic viscosity. If there is any part of the flow that is under-resolved, small-scale structures will therefore pile up there, and the code will eventually crash as a consequence of this.

In § 3.4, the focus is on finding the appropriate time scales for defining the Stokes number. The importance of this is also known from turbulent-channel (or pipe) flows experiencing turbophoresis leading to accumulation of particles in the near-wall regions (Rouson & Eaton 2001; Marchioli & Soldati 2002; Marchioli *et al.* 2008; Picano, Sardina & Casciola 2009). Furthermore, the importance of using the right time scales are also known from homogeneous and isotropic turbulent flows (Goto & Vassilicos 2006), where, for particles with response times of the order of the eddy turnover time, the particles are found to accumulate in the quiet zones between the turbulent eddies. As the cylinder immersed in the flow, in some senses, is similar to a wall, one could, for very large Reynolds numbers, experience turbophoresis of the same kind as found in the turbulent boundary layers mentioned above (Rouson & Eaton 2001; Marchioli & Soldati 2002; Marchioli *et al.* 2008; Picano *et al.* 2009). For the flows in this study, the Reynolds numbers are, however, too small for the boundary layer around the cylinder to become turbulent, and therefore there will be no turbophoresis as long as the inlet is laminar.

In this study, we have chosen to focus on laminar flows. By laminar we mean that the incoming flow and the very near wake of the object is not turbulent. Furthermore, we solve the equations only in two dimensions since basically all major flow variations are in the plane normal to the cylinder axis. The flow is nevertheless considered a three-dimensional flow such that, e.g., the particle surface is the surface of a sphere and not a cylinder. As three-dimensional effects do indeed appear for some of the Reynolds numbers considered here, in particular in the downstream wake of the cylinder, this is clearly not an exact solution. It is believed, though, that this will not have a dramatic effect on the particle deposition as long as the fluid entering the computational domain is not turbulent.

2. Numerical method

In this study, we use THE PENCIL CODE (2009), which is a high-order finite-difference code for compressible hydrodynamic flows. It is highly modular and can easily be adapted to different types of problems. The code runs efficiently under the message passing interface (MPI) on massively parallel shared- or distributed-memory computers, such as large Beowulf clusters. In THE PENCIL CODE, the fluid flow described by the Eulerian formalism, while the Lagrangian formalism is used for the particle transport. Using the Eulerian formalism for the fluid flow is a valid approximation as long as the fluid can be assumed to be a continuum and as long as the diameter of each Lagrangian particle, d, is not much smaller than the mean free path, λ, of a typical fluid molecule. When the Lagrangian particles become similar or slightly smaller in size to the mean free path of a fluid molecule, the effect of the individual fluid molecules hitting the Lagrangian particle must be taken into account by including the Stokes–Cunningham parameter to the drag law.

Since the particle deposition relies heavily on the boundary layer, it is crucial to resolve the boundary layer properly. Here, we follow the grid requirements used in Bouhairie & Chu (2007), where the first grid point is always closer to the cylinder surface than

$$\delta_1 = \frac{0.335}{\sqrt{Re}} D \tag{2.1}$$

when Re is the Reynolds number based on the mean flow velocity and the cylinder diameter.

2.1. *The fluid equations*

We assume the flow to be isothermal. The governing fluid equations are the continuity equation

$$\frac{D\rho}{Dt} = -\rho \nabla \cdot \boldsymbol{u}, \tag{2.2}$$

and the momentum equation

$$\rho \frac{D\boldsymbol{u}}{Dt} = -\nabla P + \nabla \cdot (2\mu \boldsymbol{S}), \tag{2.3}$$

where $\boldsymbol{u}$ is velocity, ρ is density, t is time and P is pressure. Also,

$$\boldsymbol{S} = \tfrac{1}{2}(\nabla \boldsymbol{u} + (\nabla \boldsymbol{u})^T) - \tfrac{1}{3} \nabla \cdot \boldsymbol{u} \tag{2.4}$$

is the traceless rate of strain tensor and

$$\frac{D}{Dt} = \frac{\partial}{\partial t} + \boldsymbol{u} \cdot \nabla \tag{2.5}$$

is the advective derivative. Furthermore, the pressure is given by the ideal gas equation of state, which, due to the isothermal flow assumption, reduces to

$$P = c_s^2 \rho, \tag{2.6}$$

where $c_s = \sqrt{\partial P / \partial \rho}$ is the speed of sound. The above equation cannot, however, be used for too large Mach numbers as the flow can then no longer be considered isothermal. As the focus of this study is on the low-Mach-number limit, one could have also used the incompressible form of the equations.

2.2. *The particle equations*

The particles are tracked using a Lagrangian formalism, where the evolution equation for the velocity is given as

$$\frac{d\boldsymbol{v}}{dt} = \frac{\boldsymbol{F}}{m_p}, \tag{2.7}$$

and for the position as

$$\frac{d\boldsymbol{x}}{dt} = \boldsymbol{v}, \tag{2.8}$$

where m_p, $\boldsymbol{v}$ and $\boldsymbol{x}$ are the mass, velocity and position of the particle's centre of mass, respectively. Furthermore, the force $\boldsymbol{F}$ is the sum of all forces acting on the particle. These forces are e.g. the drag force, Brownian diffusion, the thermophoretic force, electromagnetic forces, particle–particle forces, particle–wall forces and gravity. In this study, we restrict ourself to the drag force, i.e. $\boldsymbol{F} = \boldsymbol{F}_D$, where the drag force is given by

$$\boldsymbol{F}_D = \tfrac{1}{2}\rho C_D A |\boldsymbol{u} - \boldsymbol{v}|(\boldsymbol{u} - \boldsymbol{v})/C_c, \tag{2.9}$$

and the drag coefficient by

$$C_D = \begin{cases} 0.44, & \text{if } Re_p > 1000, \\ \dfrac{24}{Re_p}\left(1 + 0.15Re_p^{0.687}\right), & \text{if } Re_p \lesssim 1000. \end{cases} \tag{2.10}$$

The particle Reynolds number is given by $Re_p = d_p|\boldsymbol{v} - \boldsymbol{u}|/\nu$, where $d_p = 2r$ is the particle diameter, $A = \pi r^2$ is the cross-sectional area of the particle,

$$C_c = 1 + \frac{2\lambda}{d}\left(1.257 + 0.4e^{-(1.1d/2\lambda)}\right) \tag{2.11}$$

is the Stokes–Cunningham factor and λ is the mean free path for a typical molecule in the fluid. For atmospheric pressure, the mean free path is given by

$$\lambda = \nu\sqrt{\frac{\pi M}{2RT}} \tag{2.12}$$

corresponding to $\lambda = 67$ nm for air at room temperature, where M is the mean molecular mass, T is the temperature and R is the universal gas constant. The Stokes–Cunningham factor accounts for the fact that for very small particles, the surrounding medium can no longer be regarded as a continuum but rather distinct particles.

When $Re_p < 1000$, (2.9) can be written as

$$\boldsymbol{F}_D = \frac{m}{\tau_p}(\boldsymbol{u} - \boldsymbol{v}), \tag{2.13}$$

where

$$\tau_p = \frac{2mC_c}{\rho C_D \pi r^2 |\boldsymbol{u} - \boldsymbol{v}|} = \frac{8\rho_p r C_c}{3\rho C_D |\boldsymbol{u} - \boldsymbol{v}|} = \frac{Sd^2 C_c}{18\nu(1 + f_c)} \tag{2.14}$$

is the particle response time, $f_c = 0.15Re_p^{0.687}$ and $S = \rho_p/\rho$, where ρ_p is the density of the particle.

In this study, the particle Reynolds number is always rather small, reducing, to a good approximation, the drag force to the classical Stokes drag. For generality, (2.9)–(2.12) are nevertheless used throughout this paper.

As the particles are generally not exactly at the position of a grid point, some interpolation is required to determine the values of e.g. the fluid velocity and density at the position of the particle. In this study, a first-order interpolation scheme is used. Such a low interpolation order is chosen to avoid severe problems very close to the solid geometry. For a description of how the particle interpolation is handled in the vicinity of the solid geometry, see the last part of §2.4.1.

2.3. *Boundary conditions*

In all our simulations, the spanwise direction has periodic boundary conditions both for the fluid and for the particles. This means that a particle of a fluid element leaving the domain at one side is immediately inserted into the domain in the same state at the other side. In the streamwise direction, we use partially reflecting Navier–Stokes characteristic boundary conditions (NSCBC) (see Poinsot & Lele 1992) for the fluid at both the inlet and the outlet. The particles are inserted a few grid cells downstream of the fluid inlet, and are removed from the simulation when they reach the fluid outlet or hit the cylinder.
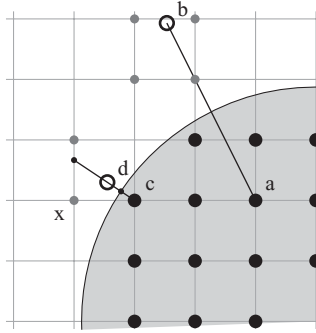
FIGURE 1. Ghost points (black) and an example of a mirror point (b). The value of the mirror point is interpolated from its four nearest neighbours (grey). The situation is slightly different for a mirror point that does not have four nearest neighbour points within the fluid (d). In this case, we make an interpolation between the nearest position at the solid–fluid interface, which is defined by the boundary conditions, and a fluid point on the first intersected grid line. This interpolation is quadratic for the radial velocity and linear for all other parameters. The value of the fluid point at the first intersected grid line is found by a linear interpolation of its nearest grid points (grey) along the grid line.

2.4. *The solid geometry*

In order to simulate the fluid flow around a solid object, like a cylinder or a sphere, or even multiple such objects, we need somehow to include these structures in the flow domain. We have chosen to work with a grid that does not conform to the boundary of the object. This enables us to use the existing solver of THE PENCIL CODE without fundamental changes due to the geometry of the object, and future generalizations and extensions, like the inclusion of multiple objects or objects with non-cylindrical shapes, will be straightforward. However, incorporating the boundary conditions formally requires a modification of the equations in the vicinity of the boundary, since the solid body does not, in general, coincide with the grid, only cutting through the Cartesian grid cells, as shown in figure 1. We can account for the solid by adding a virtual-force term to the momentum equation (2.3). This then represents the action of the solid upon the fluid and is commonly known as the immersed boundary method. Originally introduced by Peskin in the early 1970s to study flow patterns around heart valves (Peskin 2002), the term 'immersed boundary method' is now used for a large class of methods that simulate flow around boundaries on non-body conformal grids (Mittal & Iaccarino 2005).

The virtual force can be chosen so that we obtain the desired velocity distribution over the boundary of the solid, and since there are, in principle, no restrictions on this choice, a wide variety of boundary conditions can be used.

In this study, we use the discrete forcing approach, in which the equations are first discretized on a Cartesian grid without regard to the immersed boundary, and then the forcing is introduced. The advantage of using this approach is that it allows direct control over the numerical accuracy, stability and discrete conservation properties of the solver (Mittal & Iaccarino 2005).

2.4.1. *The immersed boundary method using ghost points*

Whereas smoothing can be useful when dealing with elastic boundaries, it is problematic for rigid bodies, especially at higher Reynolds numbers, where there is a need to accurately resolve the boundary layers. Using ghost points within the

solid body, we directly impose the boundary conditions on the boundary in a way that ensures a sharp wall separating the fluid and the solid. We assign properties to the ghost points based on the properties of their mirror points in the fluid. If the boundary is parallel to the grid in either direction, the situation is simple. The boundary may not coincide precisely with the midpoint between two vertices in the grid, so in order to find the mirror points, which are used to set the state of the ghost points, some interpolation is necessary. Since the mirror points, however, are well defined and always situated on the grid lines, only a simple linear interpolation of the state of the closest two grid points needs to be made.

A more difficult situation is found when the interface between the solid and the fluid is curved (figure 1). For grid lines that coincide exactly with the surface normal of the solid body, the situation is as before. On the other hand, if the curvature is too large, then the ghost points will not be well defined because there is more than one mirror point in the fluid. In order to ensure well-defined ghost points with unique mirror points, the curvature κ of the solid object surface has to be restricted by

$$\kappa < \frac{1}{3\Delta x}, \tag{2.15}$$

where Δx is the distance between two grid points. This is a consequence of using a sixth-order central difference scheme, where three grid points to either side are needed to evaluate a derivative at a given point.

When the ghost points are situated on grid lines that are not normal to the boundary (e.g. point a in figure 1), we first have to identify the normal and use this to find the mirror point. In general, the mirror point is not identical to a grid point, and the state is interpolated from its four nearest neighbours (in three dimensions, the eight nearest grid points).

Mirror points too close to the solid body to have their four nearest neighbour grid points within the fluid (point d in figure 1) are calculated using a slightly different approach. For these, we make an interpolation along the surface normal between the surface and the point where the normal intersects its first grid line inside the fluid region. The state of the latter point is found by a linear interpolation of the closest vertices along its grid line.

A similar procedure is used to avoid spurious effects when fluid (grid) points are too close to the boundary. We believe these effects arise because of the effective delocalized dependency in the finite differences. Consider, for example the fluid point x in figure 1. Calculating the central sixth-order finite difference here implies using among others the ghost point a, which, in turn, is given by the state of the mirror point b, relatively far from the original point x. The more pronounced the effect is, the closer the fluid point is to the boundary. If it is closer than some pre-defined cutoff (typically chosen to be $0.7\Delta x$), we explicitly assign a value to the fluid point based on an interpolation along the surface normal, as shown in figure 2. Here, the fluid point a is given the interpolated value between the surface point b and the grid–normal intersection point c. The intersection point c is itself interpolated from its two nearest neighbours along the grid line (the two grey points in figure 2). When finding the interpolated values close to the boundary, we use linear interpolations for all variables except for the radial velocity, where quadratic interpolation is used. The use of quadratic interpolation is verified in §3.5. The interpolated values at particle positions for particles very close to the solid geometry are found by the same approach, as described above for the fluid points.

	Re = 40		Re = 100	
	C_D	L_w	C_D	Str
Ye *et al.* (1999)	1.52	2.27	–	–
Lai & Peskin (2000)	–	–	1.4473	0.165
Kim, Kim & Choi (2001)	1.51	–	1.33	0.165
Borthwick (1986)	1.507	–	–	–
Tritton (1959)	1.58	–	1.25	–
Chern, Borthwick & Taylor (2005)	1.480	2.20	–	–
Dennis & Chang (1970)	1.522	2.35	–	–
Su, Lai & Lin (2007)	1.63	–	1.40	0.168
Pan (2006)	1.510	2.18	1.32	0.16
Tseng & Ferziger (2003)	1.53	2.21	1.42	0.164
Noor, Chern & Horng (2009)	1.560	2.219	1.4	0.167
Present study	1.537	2.27	1.328	0.166

TABLE 1. Comparison of data sets from previous studies. Only Tritton (1959) refers to an experimental study, whereas the others represent numerical studies using various methods.
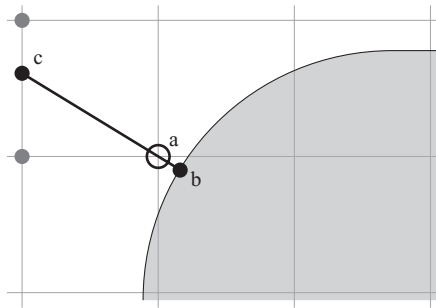

FIGURE 2. A fluid point (a) that is too close to the fluid–solid interface is calculated explicitly from an interpolation between a surface point (b) and the intersection of the surface normal with the first grid line (c). This point (c) is, in turn, the interpolated value of its two nearest neighbour vertices (grey) on the grid line.

It is likely that the effective order of the numerical scheme is somewhat lowered due to the ghost-point-based immersed boundary method.

3. Results

3.1. *Verifications of the fluid implementation*

In order to verify the accuracy of the simulations, grid-independence tests have been performed to check that the results do not change as the resolution is increased. In addition to this, the results from the Cartesian simulations have been compared with similar simulations using cylindrical, i.e. body conformal, grids.

Several studies of the flow past a stationary circular cylinder exist, and we will present here a comparison of our results with previous numerical and experimental data sets given in table 1.

For small Reynolds numbers, $Re < Re_{Kármán}$, the flow will be stationary. Williamson (1996*b*) found that $Re_{Kármán} = 49$ when the Reynolds number is based on the cylinder

diameter D and the mean flow velocity u_0 such that

$$Re = \frac{u_0 D}{\nu}. \tag{3.1}$$

For Reynolds numbers larger than $Re_{recirc} \approx 5$ and smaller than $Re_{Kármán}$, a stationary recirculation zone will exist behind the cylinder. The length of this recirculation zone l_w, normalized by the cylinder diameter, gives the normalized recirculation length $L_w = l_w/D$. In table 1, we present our measurements of L_w together with results found elsewhere in the literature, and we see that we are within the spread of the other results.

When the Reynolds number of the flow exceeds $Re_{Kármán}$, the flow becomes unsteady, and will begin to show von Kármán eddies. The non-dimensional measure of the frequency of these eddies is the Strouhal number:

$$Str = \frac{f}{1/\tau_f}, \tag{3.2}$$

where f is the frequency of the von Kármán eddies and $\tau_f = D/u_0$ is the typical fluid relaxation time. A comparison of our results with data found in the literature is shown in table 1.

The total force on the cylinder is given by the sum of the pressure and viscous forces integrated over the cylinder surface A,

$$\boldsymbol{F} = \int_A P \mathrm{d}\boldsymbol{A} + \int_A \tau \mathrm{d}\boldsymbol{A}. \tag{3.3}$$

Given that the flow is in the x-direction, and that y is the spanwise direction, the drag coefficient is given by

$$C_D = \frac{F_x}{\frac{1}{2}\rho_0 u_0^2 D H}. \tag{3.4}$$

In the above, ρ_0 is the density in the far field, H is the length of the cylinder and τ is the viscous stress tensor. Our results for the drag coefficient are presented in table 1, where for $Re = 100$, a time average is used.

It is important to note here that the recirculation length, the drag coefficient and the Strouhal number are affected both by the size of the simulation domain and by the boundary conditions used. For the results shown in table 1, the domain is $37D$ in the spanwise direction and $70D$ in the direction parallel to the flow, with smooth side walls and NSCBC (Poinsot & Lele 1992) at the inlet and outlet, as described in §2.3. Tritton (1959) is the only experimental study in table 1 and operates with an overall accuracy of the results for the drag coefficient C_D of around 6 %, but admits its results to be on the low side for the highest Reynolds number. As a whole, we find satisfactory agreement between our simulations and the various studies listed in the table.

3.2. *Impaction efficiency*

In figure 3(*a*), the instantaneous fluid streamlines of a simulation with $Re = 421$ are shown. The von Kármán eddies are clearly seen downstream of the grey circle representing the cylinder. Within the black box shown in the lower part of the plot, the particles are inserted at random positions and with a constant velocity equal to the fluid velocity at the inlet. In figure 3(*b*), it is seen that the small particles of Stokes number 0.04 follow the fluid pretty well. The exception is within the central part of the van Kármán eddies which, due to their large centrifugal forces, have been emptied of particles. Finally, figure 3(*c*) shows how the large particles of Stokes number 10
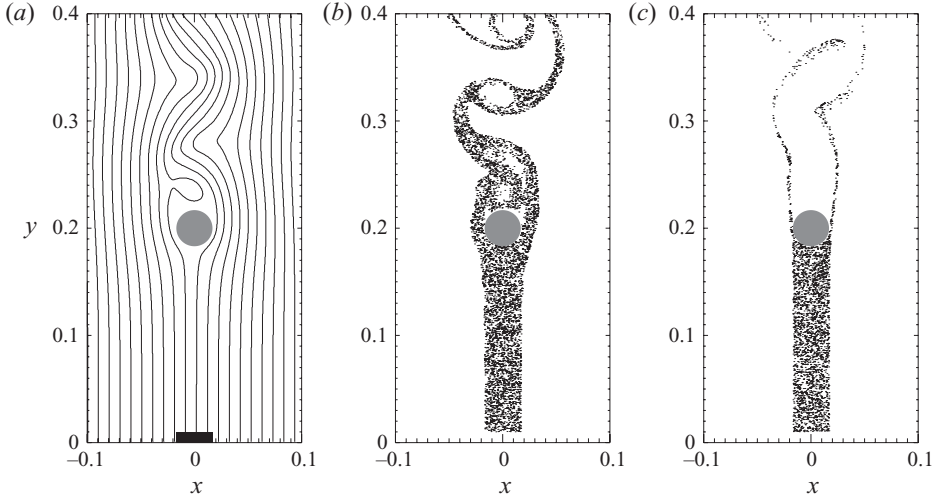
FIGURE 3. Time snapshots for $Re = 421$. The grey circle in the middle of the visualizations is the cylinder. (*a*) The fluid streamlines and the small black box in the lower part correspond to the subdomain where the particles have been inserted with a random distribution. (*b*, *c*) The particles as small black dots for Stokes number 0.04 and 10, respectively.

tend to go almost straight on, being affected by the fluid flow to a far lesser extent than the small particles.

We will now look at the particle impaction on a cylinder in a crossflow. Our main focus is the impaction efficiency $\eta = N_{impact}/N_{init}$ as a function of Stokes number

$$St = \frac{\hat{\tau}_p}{\hat{\tau}_f}, \qquad (3.5)$$

where N_{impact} is the number of particles impacting on the surface of the cylinder, N_{init} is the number of particles initially moving in the direction of the cylinder and

$$\hat{\tau}_p = \frac{Sd^2}{18\nu} \qquad (3.6)$$

is the particle relaxation time based on the pure Stokesian drag. Here,

$$\hat{\tau}_f \equiv \frac{\tau_f}{2} = \frac{D}{2u_0} \qquad (3.7)$$

is the fluid time scale, for which we have chosen to follow a different convention than in (3.2). It is important to note that in the filter community the Stokes number is normally defined as $St = \hat{\tau}_p/\tau_f$, while in the boiler community, (3.5) is used. Please note that (3.6) is found from setting $Re_p = 0$ in (2.14), i.e. by assuming that the particles are co-moving with the fluid. The reason for doing this is that there is no unique value of Re_p throughout the flow ($Re_p = 0$ is indeed the correct value at e.g. the inlet). Furthermore, the simplification of assuming $\lambda/d \ll 0$ is made such that $C_c \simeq 1$.

Initially, we run a fluid simulation without any particles until it is statistically stationary with respect to the mean vorticity and the root-mean-square velocity of the flow and to drag on the cylinder. This simulation is then used as the initial condition for the fluid field for the simulations with particles. The particles are fed in at the fluid inlet at a constant rate for a total time t_{inlet}. It is important that $t_{inlet} > t_{Kármán}$, where

$t_{Kármán} = D/(u_0 Str)$ is the period of one von Kármán eddy. In all our simulations, we use $t_{inlet} \simeq 3 t_{Kármán}$. After having fed in all the particles, we let the simulation run until all particles have left the domain. This happens either by the particles hitting the cylinder and thereby being captured, or by the particles crossing the outlet boundary. As the smallest particles might get trapped in the wake behind the cylinder, or in the boundary layer very close to the cylinder, we will normally have to run for much longer than $t_{inlet} + t_{flow}$, where $t_{flow} = L/u_0$ is the flow-through time and L is the total length of the domain.

For the remaining results, we have used a domain size of $6D \times 12D$, where the cylinder is situated in the centre of the domain, sufficiently far from the inlet so that the flow at the inlet should be unaffected by the cylinder. Because of the periodic boundary conditions, the width of the domain can be interpreted as the spacing between cylinders in an infinite array, and the impaction efficiency will depend on this spacing due to its restrictions on the flow. It is known that increasing the spacing will asymptotically decrease the impaction efficiency (Konstandopoulos, Labowsky & Rosner 1993), but the effect is considered small when increasing the domain width beyond our chosen size. The inlet velocity and cylinder diameter are kept constant. Consequently, the Reynolds number is varied by changing the viscosity. For a given Stokes and Reynolds number, the particle diameter is determined by

$$\frac{d_p}{D} = 3\sqrt{\frac{St}{SRe}}, \tag{3.8}$$

thus the particle size is increasing with increasing Stokes number.

The Reynolds numbers considered range from 20 up to 6600. It is well known (Williamson 1996*a*,*b*) that for Reynolds numbers below $\sim$190 the flow is perfectly two-dimensional. As the Reynolds number is increased, the shear layer downstream of the cylinder will gradually start to develop turbulent structures. For very large Reynolds numbers, of the order of 2×10^5, even the boundary layer of the cylinder becomes turbulent. By the fact that only two-dimensional simulations are performed in this study, it is clear that three-dimensional effects, such as turbulence and coherent streamwise vorticity, will not be reproduced in the wake. This may have an effect on the vortices causing the back-side impaction for the larger Reynolds numbers, and consequently, it may affect the back-side impaction. As no turbulence is generated in the boundary layer around the cylinder for the Reynolds numbers considered, the neglect of the third dimension is not expected to have any effect on the front-side impaction.

In all of the following, we have set the particle–fluid density ratio to $S = 1000$ and the Mach number to $Ma = u_0/c_s = 0.25$. As stated in §2.1, the Mach number must not be too large for the isothermal approximation to hold; however, at the same time, the Mach number should not be too small, as that will decrease the time step and consequently increase the CPU cost. It has been found that decreasing the Mach number to a number smaller than 0.25 does not have any significant effect on the particle deposition.

The number of grid points used are 512×1024, 1024×2048 and 2048×4096 for $Re < 1000$, $Re = 1685$ and $Re = 6600$, respectively. These resolutions have been chosen after having run grid-independence tests, which showed that increasing the resolutions even further did not have any significant effect on the particle impaction.

By decreasing the resolution, the impaction efficiency for the smallest particles does increase above the grid-independent values, while the fluid flow and the impaction efficiency of the largest particles are essentially unchanged. The reason for this is that
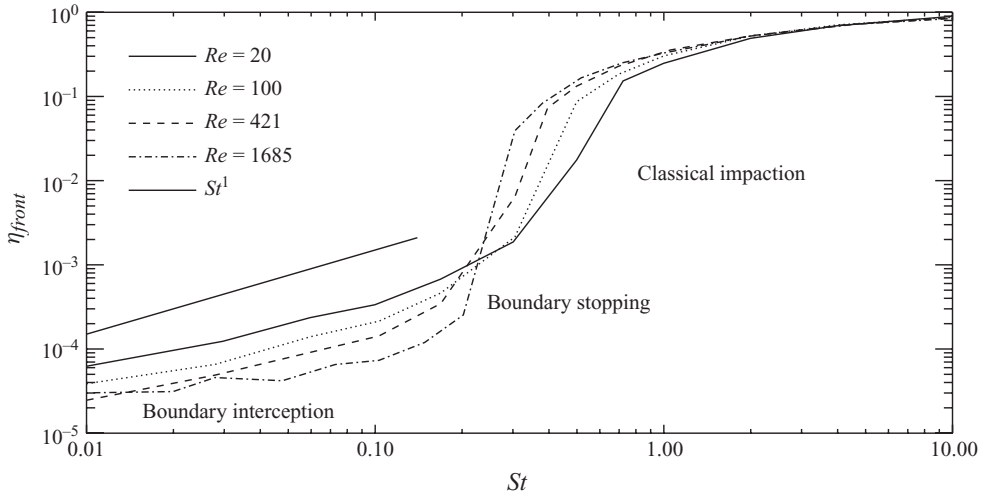
FIGURE 4. Impaction efficiency on the front side of the cylinder as function of Stokes number for different Reynolds numbers.

the smallest particles are extremely sensitive to the boundary layer very close to the cylinder, and a small inaccuracy there leads to incorrect impaction efficiencies. The fluid flow itself, together with the larger particles, is not significantly influenced by the very near boundary layer, and is therefore unaffected by the decreased resolution. Decreasing the resolution even further will, however, at some point, unavoidably lead to incorrect results also for the larger particle impaction rates and the fluid flow. Eventually, it will even make the code crash as the velocity gradients are no longer properly resolved, leading to numerical wiggles and code blowup.

3.3. *Front-side impaction*

In this subsection, we will look at the particle impaction on the front side of the cylinder. From figure 4, we see that there is a Reynolds-number dependency on the impaction efficiency. This is, however, not due to a Stokesian versus non-Stokesian drag (Israel & Rosner 1983), which is a pure-particle-Reynolds-number effect giving an effective Stokes number different from the classical one. For the parameters used in this study, the Stokes correction factor is very close to unity, and consequently the effective Stokes number, as defined in Israel & Rosner (1983), is essentially equal to the classical Stokes number.

The Reynolds-number effect seen here is due to the fact that the flow around the target can not be represented by a non-viscous model (Golovin & Putnam 1962). The effect of this is seen clearly in figure 5(*a*), where the line labelled 'IR' represents the non-viscous approximation of Israel & Rosner (1983). Here, it is seen that the larger the Reynolds number, the closer the results are to the results of Israel & Rosner (1983), which is natural since the non-viscous approximation represent an infinite Reynolds number.

In figure 5(*b*), the result with $Re = 20$ is compared to empirical fitting functions with the same Reynolds number found by Suneja & Lee (1974) and Schweers *et al.* (1994), while in figure 5(*c*) the result for $Re = 100$ is compared with corresponding data from Suneja & Lee (1974) and Muhr (1976), and in figure 5(*d*) the $Re = 421$ result is compared with the fitting function of Muhr (1976). For all the above comparisons, we see relatively good agreements between the results found in this study and the
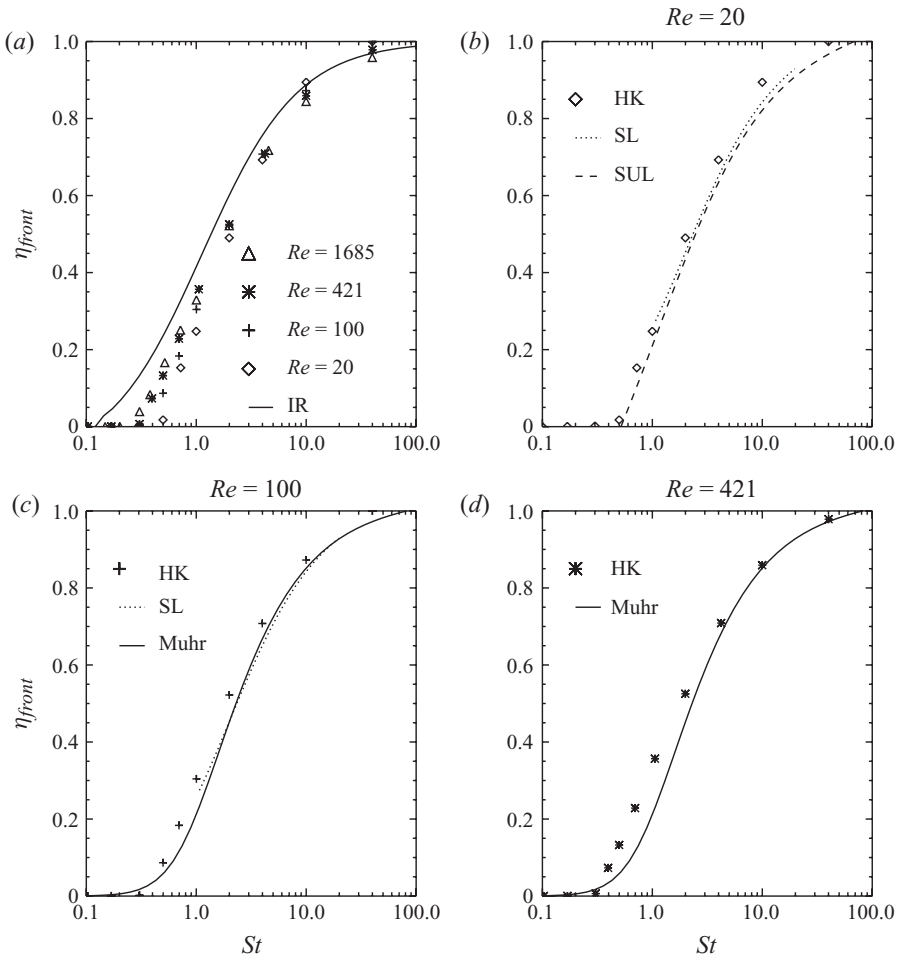
FIGURE 5. Impaction efficiency as function of Stokes number for different Reynolds numbers. The lines marked SL, SUL, Muhr and IR are functions from the work of Suneja & Lee (1974), Schweers *et al.* (1994), Muhr (1976) and Israel & Rosner (1983), respectively. Our results are marked HK.

available empirical fitting functions. The large deviations are found for the two larger Reynolds numbers at Stokes numbers around unity.

From figure 4, we see that the impaction efficiency is monotonically decreasing with decreasing Stokes number. It is seen that there are three different modes in this plot. The first mode is the classical impaction mode, where the impaction efficiency depends almost entirely on the Stokes number, and the Reynolds number has only a barely visible effect. This mode exists from infinite Stokes numbers down to Stokes number of 0.7 for $Re = 20$ and to 0.3 for $Re = 1685$. After this classical mode, there is the boundary stopping mode, where the particles start lacking sufficient inertia to penetrate the boundary layer. This mode exists for $0.3 < St < 0.7$ for $Re = 20$, and for $0.2 < St < 0.3$ for $Re = 1685$. The last mode is the boundary interception mode where the particles follow the fluid flow almost perfectly, but some of them are still impacting due to their finite radii. It can be mentioned that above Stokes numbers of around 5, in the classical mode, the small-Reynolds-number simulations have

slightly higher impaction efficiency than the higher Reynolds-number simulations, while below Stokes number 5, the opposite is true. This is due to the fact that at high Stokes numbers, interception is the dominating impaction mechanism. At large Stokes numbers, the particles are almost unaffected by the fluid, and the impaction efficiency can be approximated by the no-force expression in (1.1),

$$\eta(St \gg 1) \approx 1 + R_i. \tag{3.9}$$

Here, the interception parameter is given by (3.8),

$$R_i = 3\sqrt{\frac{St}{SRe}}, \tag{3.10}$$

thus leading to larger impaction efficiencies for smaller Reynolds numbers, given that the Stokes number is constant.

3.4. *A modified Stokes number*

The Stokes number is the ratio of the particle relaxation time to the time it takes for the fluid to change direction as it approaches the obstacle. The classical way of determining the particle relaxation time and the typical fluid time scale yields the Stokes number as given in (3.5).

The fluid relaxation time is given as

$$\tau_f = \frac{L}{u_0}, \tag{3.11}$$

where L is a typical length scale in the system. Typically, $L = D$, which is a good approximation when the viscous effects are negligible. In the case of small Reynolds and Stokes numbers, however, we cannot neglect the viscous effects as the viscous boundary layer tends to set up a 'shield' between the obstacle and the particles in the flow. In the case of large Stokes numbers, the viscous boundary layer is not important as the particle will have enough inertia to penetrate the boundary layer anyway. As the particle inertia decreases, the importance of the boundary layer for shielding the cylinder increases. By looking at the gradient of the radial velocity on the centreline upstream of the cylinder, $\mathrm{d}u_r/\mathrm{d}r$, a fluid time scale based on this stagnation point flow can be found as

$$\tau_{f,grad} = \left(\frac{\mathrm{d}u_r}{\mathrm{d}r}\right)^{-1}. \tag{3.12}$$

In figure 6, this is found to scale with Reynolds number as

$$\tau_{f,grad} \approx \tau_{f,pot}(1 + B' Re^{-1/2}), \tag{3.13}$$

where $B' = 4.45$ is a scaling parameter and $\tau_{f,pot}$ is the corresponding time scale based on a linearized potential-flow theory. In all of the above, the gradient of the radial velocity is measured between the point where the radial velocity is 40 % of the mean velocity and the cylinder surface,

$$\frac{\mathrm{d}u_r}{\mathrm{d}r} = \left.\frac{0 - u_r}{r_c - r}\right|_{u_r = 2u_0/5}. \tag{3.14}$$

The potential-flow time scale $\tau_{f,pot}$ is found from the same expression, but using $u_{r,pot} = -u_0(1 - r_c^2/r^2)$ as the radial velocity.
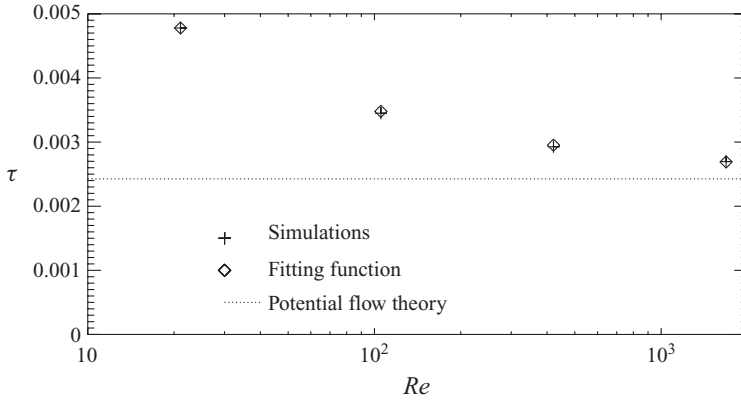
FIGURE 6. The time scale based on the front-side velocity gradient, as defined in (3.12) (+) plotted together with the fitting function defined in (3.13) (◇). The time scale based on the front-side gradient of a potential flow is shown as the dotted line, and we see that the simulated results tend to approach this value for large Reynolds numbers.
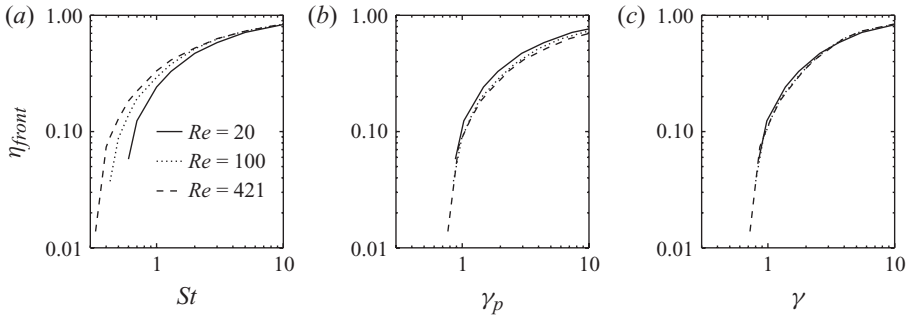

FIGURE 7. Impaction efficiency as function of Stokes number (*a*), γ_p (*b*) and γ (*c*) for different Reynolds numbers. Here, interception is neglected, i.e. the particle is regarded as having impacted when the particle centre is in contact with the cylinder surface.

A new non-dimensional number can now be defined as

$$\gamma_p = \frac{\hat{\tau}_p}{\tau_{f,grad}}. \tag{3.15}$$

In figure 7, the impaction efficiency as a function of the Stokes number is shown for the case where interception is neglected. This can be interpreted as a thought situation where the particles are treated as point-like objects, and it corresponds to dropping the interception parameter R_i in (1.1) and (3.9). When only counting impaction for particles whose centre is in contact with the cylinder surface, an impaction efficiency that approaches unity in the large-Stokes-number limit results. In figure 7(*b*), the impaction efficiency as a function of the new number γ_p is shown. It is seen, as argued in the beginning of this section, that this new number gives overlapping lines for small particles, but not for larger particles. For the larger particles, we see in figure 7(*a*) that using the classical Stokes number gives better results. It is therefore suggested that a new non-dimensional number is found as a smooth combination of γ_p and *St*. Several smoothing functions f_s can be suggested such that

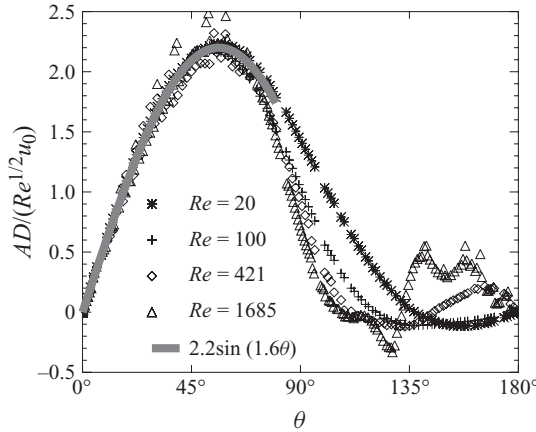$$\gamma = St f_s + (1 - f_s)\gamma_p \tag{3.16}$$

FIGURE 8. Here, we plot $1/B$ as a function of the angle θ. We see that $B \approx 1/2.2 \approx 0.45$ at its minimum, corresponding to the minimum boundary layer thickness. The solid line is the fitting function defined in (3.23).

can be used as a modified Stokes number. The choice $f_s = \tanh(St/5)$, used in figure 7(c), provides the data to collapse rather well onto one curve.

3.5. *The small-Stokes-number impaction efficiency*

Assume that the particles are so small that they follow the flow perfectly. Naïvely one would then think that the capture efficiency is given by

$$\eta = \frac{d}{D}. \tag{3.17}$$

In the case of non-vanishing viscosity, this is not the case as the viscosity tends to set up a boundary layer. For the Reynolds number considered here, this boundary layer will be laminar. As a first approximation, the tangential velocity in the boundary layer is given by

$$u_\theta = A\hat{x}, \tag{3.18}$$

where A is a Reynolds-number-dependent constant and $\hat{x}$ is the normal distance from the surface. Following Prandtl's concept of thin boundary layers, we use the following expression for the boundary layer thickness,

$$\delta = \frac{BD}{\sqrt{Re}}, \tag{3.19}$$

to find

$$A = \frac{u_0\sqrt{Re}}{BD}, \tag{3.20}$$

where B is a non-Reynolds-number-dependent constant. In figure 8, we plot $1/B$ found from (3.20), where we have measured the value of $A = u_\theta/\hat{x}$ at the grid points close to the solid surface. The angle θ is 0 at the stagnation point and increases clockwise around the cylinder. From the plot, we find that $B \approx 0.45$ at its minimum.

By fitting a sine to the values of $1/B$, we find a best fit of $1/B = 2.2\sin(1.6\theta)$ in the range of $0° < \theta < 80°$, which yields

$$\frac{\partial u_\theta}{\partial \hat{x}} = A = \alpha f(\theta), \tag{3.21}$$

where

$$\alpha = \frac{u_0 \sqrt{Re}}{D} \tag{3.22}$$

and

$$f(\theta) = 2.2 \sin(1.6\theta). \tag{3.23}$$

By assuming incompressibility, the continuity equation (2.2) reduces to

$$\frac{\partial u_r}{\partial r} + \frac{1}{r} \frac{\partial u_\theta}{\partial \theta} = 0 \tag{3.24}$$

in cylindrical coordinates. By requiring the boundary layer to be thin compared to the radius r_c of the cylinder, this reduces further to

$$\frac{\partial u_r}{\partial \hat{x}} + \frac{1}{r_c} \frac{\partial u_\theta}{\partial \theta} = 0. \tag{3.25}$$

Substituting (3.21) into (3.18) gives

$$u_\theta = \alpha f \hat{x}, \tag{3.26}$$

which can be differentiated by θ to yield

$$\frac{\partial u_\theta}{\partial \theta} = \alpha \hat{x} \frac{\partial f}{\partial \theta}. \tag{3.27}$$

By using the above equation together with (3.25), an expression for the velocity in the radial direction is found as follows:

$$u_r = -\int_0^{\hat{x}} \frac{1}{r_c} \frac{\partial u_\theta}{\partial \theta} d\hat{x}' = -\frac{1}{2r_c} \alpha \hat{x}^2 \frac{\partial f}{\partial \theta}. \tag{3.28}$$

The above equation justifies the square interpolation used for the radial velocity very close to the boundary, as described in §2.4.1. This only holds within the very thin boundary layer, whereas for the stagnation point flow, a linear radial velocity must be used, as in (3.14).

For small angles, i.e. at positions close to the front stagnation point, the radial velocity in the boundary layer will be directed towards the cylinder surface. When $\partial f / \partial \theta$ becomes 0, we have reached the point where the boundary layer is the thinnest, and from this point onwards the radial velocity becomes positive. A particle which has not yet reached the surface at this angle will not reach the front surface at all. By the fit of $f(\theta)$ from (3.23), we find that this happens at $\theta \approx 56°$. This is confirmed by figure 9, where the maximum angle of impaction is between $40°$ and $60°$ for very small Stokes numbers. Due to rather poor statistics, these numbers do, however, have rather large error bars, and we believe that is also the reason why the result for $Re = 1685$ is lower than the others.

The total volume flow in the boundary layer, inside r_p, is

$$\dot{V}_b = H \int_0^{r_p} u_\theta \, d\hat{x}' = \tfrac{1}{2} H \alpha f(\theta) r_p^2, \tag{3.29}$$

where H is the length of the cylinder. Furthermore, we know that the total volume flow inserted between the axis and Δx away from the axis far upstream is

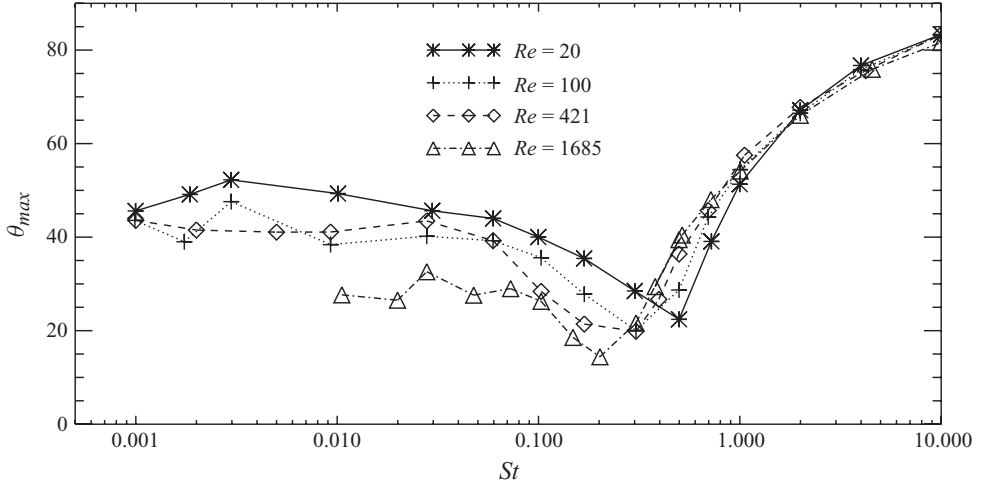$$\dot{V}_u = H u_0 \Delta x. \tag{3.30}$$

FIGURE 9. The maximum angular position of impact on the cylinder, θ_{max}, as a function of Stokes number for different Reynolds numbers.
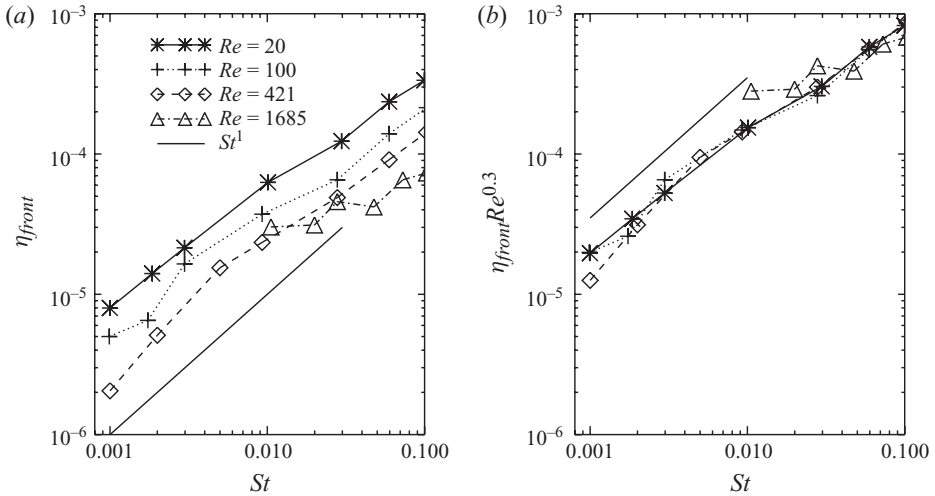

FIGURE 10. Impaction efficiency as function of Stokes number for different Reynolds numbers.

By setting $\dot{V}_u = \max(\dot{V}_b)$, we find

$$\eta = \frac{\Delta x}{r_c} = \frac{\sqrt{Re}}{4}\left(\frac{r_p}{r_c}\right)^2 f_{max}, \qquad (3.31)$$

where $f_{max} = 2.2$. From this, we can deduce

$$\eta Re^{1/2} = \frac{9 f_{max}}{4S} St. \qquad (3.32)$$

In figure 10(a), we show the classical impaction efficiency as a function of the Stokes number, while in figure 10(b), we show the impaction efficiency times the Reynolds number to the power of 0.3, which gave the best fit with the data available. It is not clear why the power is not 1/2 as found in (3.32), but one possible explanation is the

fact that (3.32) assumes a stationary flow. Due to the presence of von Kármán eddies, all the simulations with $Re > 20$ do, however, show strong transient features. This is expected to lead to a deviation from the 1/2 scaling for the following reason. Since the flow is periodically shifted to either side by the vortex shedding, the particles are accordingly pushed sideways. In turn, at each cycle there may be particles moving close enough to the cylinder to be intercepted, particles that in a stationary flow would instead follow the flow past the cylinder. Hence, it is reasonable to assume that the impaction efficiency is slightly higher than expected from arguments assuming stationary flow, and a higher Reynold number should make this effect more pronounced. Consequently, a lower exponent than 1/2 will be required to obtain the data collapse in figure 10.

3.6. *Back-side impaction*

The impaction efficiency on the back side of the cylinder is shown in figure 12 for different Reynolds numbers. For Reynolds numbers 20 and 100, no impaction on the back side was found. This becomes obvious as we investigate the reason for back-side impaction.

In this study, since we only consider the drag force, the back-side impaction cannot result from either Brownian motion, gravity or thermophoresis as would be a classical explanation. Instead, the impaction results from particles having large enough inertia in the direction towards the back side of the cylinder, i.e. in the direction opposite to the main flow, to reach the cylinder surface. The particles can only gain inertia in this direction from the eddies in the wake of the cylinder. For an eddy to transfer a significant amount of inertia to the particle, the eddy turnover time, τ_{eddy}, cannot be much smaller than the particle relaxation time, τ_p, as it will then be too fast to accelerate the particle. Furthermore, it must not be so slow that $\tau_p \ll \tau_{eddy}$ as the particle will then follow the eddy perfectly and not be thrown out of it towards the wall. Consequently, the eddy Stokes number, $St_{eddy} = \tau_p / \tau_{eddy}$, must be of the order of unity to see any impaction on the lee side of the cylinder.

In figure 11, we show the instantaneous vorticity field on the back side of the cylinder for different Reynolds numbers. It is clearly seen that the higher the Reynolds number, the larger the magnitude of the vorticity is. The large vorticity magnitude is one of two effects which leads to larger impaction for a given Stokes number St. This is because a large vorticity means large velocities, which may accelerate the particle to such a degree that it is thrown into the back side of the cylinder, provided that the wake dimension is large enough to maintain τ_{eddy} within the appropriate range. The other effect is the fact that for large Reynolds numbers the distance over which the local fluid flow in the direction of the cylinder surface will be deflected away from the cylinder is smaller. This distance can be thought of as a local boundary layer. Hence, for large Reynolds numbers, particles may more easily penetrate through to the cylinder and impact. From figure 11, it is also seen that the large-Reynolds-number simulations have more small-scale vorticity than the small-Reynolds-number simulations. This allows also smaller particles to be captured as these small eddies have shorter eddy turnover times, leading to eddy Stokes numbers of order unity also for the smaller particles. This effect is seen in figure 12 where the large-Reynolds-number simulations show back-side impaction also for smaller Stokes numbers. Please keep in mind, however, that, as discussed in §3.2, the higher Reynolds numbers considered here will show turbulence in the downstream wake in three dimensions. This effect is naturally not found in the two-dimensional simulations used here, and this may therefore have an effect on the presented results of the back-side impaction.
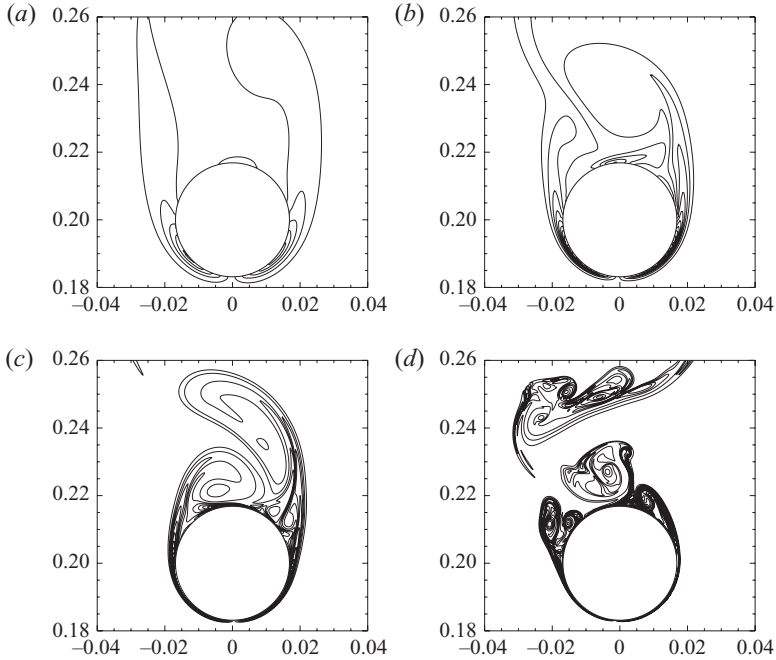
FIGURE 11. Vorticity contours near the cylinder for simulations with Reynolds numbers of
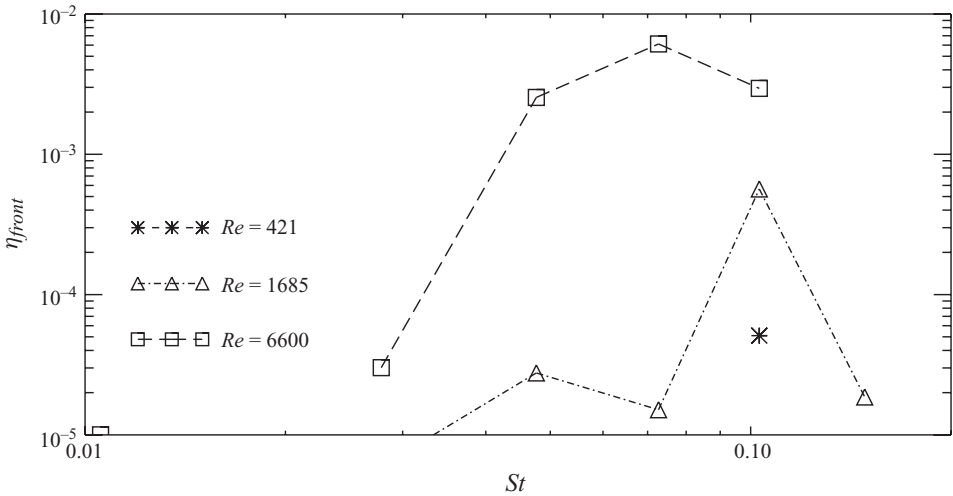100 (*a*), 421 (*b*), 1685 (*c*) and 6600 (*d*).

FIGURE 12. Impaction efficiency at the back side of the cylinder as a function of Stokes
number for different Reynolds numbers.

From the above argument, we conclude that there does not appear to be any finite
lower limit on the Stokes number for which particle impaction on the back side of
the cylinder can be found, as long as the Reynolds number is large enough.

There does, however, seem to be an upper limit on the Stokes number for back-side
impaction, as a given cylinder cannot be the source of eddies larger than its own
size in the spanwise direction, which means that large particles will always have

eddy Stokes numbers significantly larger than unity. This limit appears to be around $St \approx 0.13$.

Li *et al.* (2008) also focused on the back-side impaction, but their focus was on the angle of impaction, and not on impaction as a function of Stokes and Reynolds numbers. Their results are therefore not very easily comparable with the current results. Ilias & Douglas (1989) use a simulation code with artificial viscosity, but they did not see any back-side impaction. This is, however, reasonable as their codes probably were too viscous to contain strong small-scale vortices.

4. Conclusion

In this study, we have studied particle impaction on a cylinder as a function of the Stokes and Reynolds numbers. The only force on the particles is the drag force from the fluid. Qualitatively, the front-side impaction efficiency has the same functional dependency on the Stokes number for all Reynolds numbers, with three different modes for different ranges of the Stokes number.

The low-Stokes-number regime is characterized by an effective shielding of the cylinder by the boundary layer so that the only contribution to the front-side impaction efficiency comes rather surprisingly from interception of the particles. We have dubbed this 'the boundary interception mode' and it is an effect of the finite size of the particles, as point-like particles would follow the flow perfectly past the cylinder without any impaction. For intermediate Stokes numbers, there is first a transition regime, 'the boundary stopping mode', in which the boundary layer is still important, but the inertia of the particles begins to play a role for the impaction. The larger particles with even higher Stokes numbers are only barely influenced by the boundary layer, and their initial inertia is the determining factor for their impaction efficiency. We have used the term 'classical impaction mode' for this regime. In the limit when the Stokes number goes to infinity, the particles are unaffected by the fluid, but below this limit both the Stokes number and the fluid Reynolds number are parameters determining the impaction efficiency. In the classical impaction mode, we have, however, demonstrated that the Reynolds-number dependency can be accounted for by modifying the Stokes number according to a measured effective time scale of the fluid.

As opposed to the front side, the back-side impaction is critically dependent on the Reynolds number. We observe no impaction on the back side of the cylinder for the two smallest Reynolds numbers studied, $Re = 100$ and 20, and for the higher Reynolds numbers, we observe impaction only up to a limiting Stokes number of around 0.13. We understand this in terms of constraints on the dimensions of, and also the vorticity in, the wake behind the cylinder that needs to be fulfilled for particles to impact.

It is clear that the details of the viscous boundary layer is crucial for the understanding of the impaction efficiency of the smallest particles, and a high numerical accuracy is necessary in order to simulate and study this phenomenon. Because, almost counter-intuitively, the finite radii of the particles are very important for the impaction in this boundary interception mode, an improved model for the forces on the particles should be adapted in future studies. Whereas electromagnetic forces and chemical effects are material-dependent, Brownian diffusion and lift forces are not, and it would be interesting to see how such generic forces affect the impaction efficiency. Particle–particle interaction can also be left out because this depends on the number density of the particles and therefore is not as important for the general

mechanisms of particle impaction. It is, however, not fully understood what a turbulent inflow would do to the impaction efficiency, but it seems likely that some kind of turbophoresis will show up at specific flow and particle parameters. This should be studied in the future.

REFERENCES

BAXTER, L. L. 1990 Coal combustion science: quarterly progress report. *Tech. Rep.* SAND 90-8247. Sandia National Laboratory.

BORTHWICK, A. 1986 Comparison between two finite-difference schemes for computing the flow around a cylinder. *Intl J. Numer. Methods Fluids* **6** (5), 275–290.

BOUHAIRIE, S. & CHU, V. H. 2007 Two-dimensional simulation of unsteady heat transfer from a circular cylinder in crossflow. *J. Fluid Mech.* **570**, 177–215.

CHERN, M. J., BORTHWICK, A. G. L. & TAYLOR, R. E. 2005 Pseudospectral element model for free surface viscous flows. *Intl J. Numer. Methods Heat Fluid Flow* **15** (6), 517–554.

DENNIS, S. C. R. & CHANG, G.-Z. 1970 Numerical solutions for steady flow past a circular cylinder at Reynolds numbers up to 100. *J. Fluid Mech. Digit. Arch.* **42** (3), 471–489.

GOLOVIN, M. N. & PUTNAM, A. A. 1962 Inertial impaction on single elements. *Ind. Engng Chem. Fundam.* **1**, 264–273.

GOTO, S. & VASSILICOS, J. C. 2006 Self-similar clustering of intertial particles and zero-acceleration points in fully developed two-dimensional turbulence. *Phys. Fluids* **18**, 115103.

HUANG, L. Y., NORMAN, J. S., POURKASHANIAN, M. & WILLIAMS, A. 1996 Prediction of ash deposition on superheater tubes from pulverized coal combustion. *Fuel* **75**, 271–279.

ILIAS, S. & DOUGLAS, P. L. 1989 Inertial impaction of aerosol particles on cylinders at intermediate and high Reynolds numbers. *Chem. Engng Sci.* **44**, 81–99.

INGHAM, D., HILDYARD, M. & HEGGS, P. 1990 On the critical Stokes' number for particle transport in potential and viscous flows near bluff bodies. *J. Aerosol Sci.* **21**, 935–946.

ISRAEL, R. & ROSNER, D. 1983 Use of a generalized Stokes number to determine the aerodynamical capture efficiency of non-Stokesian particles from a compressible gas flow. *Aerosol Sci. Technol.* **2**, 45–51.

KASPER, G., SCHOLLMEIER, S., MEYER, J. & HOFERER, J. 2009 The collection efficiency of a particle-loaded single filter fiber. *J. Aerosol Sci.* **40** (12), 993–1009.

KIM, J., KIM, D. & CHOI, H. 2001 An immersed-boundary finite-volume method for simulations of flow in complex geometries. *J. Comput. Phys.* **171** (1), 132–150.

KONSTANDOPOULOS, A. G., LABOWSKY, M. J. & ROSNER, D. E. 1993 Inertial deposition of particles from potential flows past cylinder arrays. *J. Aerosol Sci.* **24** (4), 471–483.

LAI, M.-C. & PESKIN, C. S. 2000 An immersed boundary method with formal second-order accuracy and reduced numerical viscosity. *J. Comput. Phys.* **160** (2), 705–719.

LI, X., ZHOU, H. & CEN, K. 2008 Influences of various vortex structures on the dispersion and deposition of small ash particles. *Fuel* **87**, 1379–1382.

LOEHDEN, D., WALSH, P. M., SAYRE, A. N., BEER, J. M. & SAROFIM, A. F. 1989 Generation and deposition of fly ash in the combustion of pulverised coal. *J. Inst. Energy* pp. 119–127.

MARCHIOLI, C. & SOLDATI, A. 2002 Mechanisms for particle transfer and segregation in a turbulent boundary flow. *J. Fluid Mech.* **468**, 283–315.

MARCHIOLI, C., SOLDATI, A, KUERTEN, J. G. M., ARCHEN, B., TANIRE, A., GOLDENSOPH, G., SQUIRES, K. D., CARGNELUTTI, M. F. & PORTELA, L. M. 2008 Statistics of particle dispersion in direct numerical simulations of wall-bounded turbulence: results of an international collaborative benchmark test. *Intl J. Multiph. Flow* **34**, 879–893.

MITTAL, R. & IACCARINO, G. 2005 Immersed boundary methods. *Annu. Rev. Fluid Mech.* **37** (1), 239–261.

MUHR, W. 1976 Theoretical and experimental investigation of particle deposition in fibrous filters by field and inertial forces. Dissertation, Institut für Mechanische Verfahrenstechnik und Mechanik, Universität Karlsruhe, Karlsruhe, Germany.

NOOR, D., CHERN, M.-J. & HORNG, T.-L. 2009 An immersed boundary method to solve fluid–solid interaction problems. *Comput. Mech.* **44** (4), 447–453.

PAN, D. 2006 An immersed boundary method on unstructured Cartesian meshes for incompressible flows with heat transfer. *Numer. Heat Transfer Part* B *Fundam.: Intl J. Comput. Methodol.* **49** (3), 277–297.

THE PENCIL CODE 2009 http://www.nordita.org/software/pencil-code

PESKIN, C. S. 2002 The immersed boundary method. In Acta Numerica (ed. A. Iserles), vol. 11, pp. 479–517. Cambridge University Press.

PICANO, F., SARDINA, G. & CASCIOLA, C. M. 2009 Spatial development of particle-laden turbulent pipe flow. *Phys. Fluids* **21**, 093305.

POINSOT, T. J. & LELE, S. K. 1992 Boundary conditions for direct simulations of compressible viscous flows. *J. Comput. Phys.* **101** (1), 104–129.

ROUSON, D. W. I. & EATON, J. K. 2001 On the preferential concentration of solid particles in turbulent channel flow. *J. Fluid Mech.* **428**, 149–169.

SCHWEERS, E., UMHAUER, H. & LÖFFLER, F. 1994 Experimental investigations of particle collection on single fibres of different configurations. *Part. Syst. Charact.* pp. 275–283.

SU, S.-W., LAI, M.-C. & LIN, C.-A. 2007 An immersed boundary technique for simulating complex flows with rigid boundary. *Comput. Fluids* **36** (2), 313–324.

SUNEJA, S. K. & LEE, C. H. 1974 Aerosol filtration by fibrous filters at intermediate Reynolds numbers ($\leqslant 100$). *Atmos. Environ.* **8**, 1081–1094.

TRITTON, D. J. 1959 Experiments on the flow past a circular cylinder at low Reynolds numbers. *J. Fluid Mech. Digit. Arch.* **6** (4), 547–567.

TSENG, Y.-H. & FERZIGER, J. H. 2003 A ghost-cell immersed boundary method for flow in complex geometry. *J. Comput. Phys.* **192** (2), 593–623.

WILLIAMSON, C. H. K. 1996a Three-dimensional wake transition. *J. Fluid Mech. Digit. Arch.* **328**, 345–407.

WILLIAMSON, C. H. K. 1996b Vortex dynamics in the cylinder wake. *Annu. Rev. Fluid Mech.* **28**, 477–539.

YE, T., MITTAL, R., UDAYKUMAR, H. S. & SHYY, W. 1999 An accurate Cartesian grid method for viscous incompressible flows with complex immersed boundaries. *J. Comput. Phys.* **156** (2), 209–240.

YILMAZ, S. & CLIFFE, K. R. 2000 Particle deposition simulation using the CFD code fluent. *J. Inst. Energy* pp. 65–68.